A Three-Component Scattering Model for Polarimetric SAR Data

Anthony Freeman, *Senior Member, IEEE*, and Stephen L. Durden

Abstract— An approach has been developed that involves the fit of a combination of three simple scattering mechanisms to polarimetric SAR observations. The mechanisms are canopy scatter from a cloud of randomly oriented dipoles, even- or double-bounce scatter from a pair of orthogonal surfaces with different dielectric constants and Bragg scatter from a moderately rough surface. This composite scattering model is used to describe the polarimetric backscatter from naturally occurring scatterers. The model is shown to describe the behavior of polarimetric backscatter from tropical rain forests quite well by applying it to data from NASA/Jet Propulsion Laboratory's (JPL's) airborne polarimetric synthetic aperture radar (AIRSAR) system. The model fit allows clear discrimination between flooded and nonflooded forest and between forested and deforested areas, for example. The model is also shown to be usable as a predictive tool to estimate the effects of forest inundation and disturbance on the fully polarimetric radar signature.

An advantage of this model fit approach is that the scattering contributions from the three basic scattering mechanisms can be estimated for clusters of pixels in polarimetric SAR images. Furthermore, it is shown that the contributions of the three scattering mechanisms to the HH, HV, and VV backscatter can be calculated from the model fit. Finally, this model fit approach is justified as a simplification of more complicated scattering models, which require many inputs to solve the forward scattering problem.

I. INTRODUCTION

CLASSIFICATION, decomposition, and modeling of polarimetric synthetic aperture radar (SAR) data has received a great deal of attention in recent literature. The objective behind these efforts is to better understand the scattering mechanisms that give rise to the polarimetric signatures seen in SAR image data.

A major problem in analyzing polarimetric SAR data, such as that produced by the NASA/Jet Propulsion Laboratory (JPL) airborne polarimetric SAR (AIRSAR) and Spaceborne Imaging Radar-C (SIR-C) systems is in understanding the scattering mechanisms that give rise to features in the different polarization parameters. Researchers, on examining some polarimetric SAR data from their scene of interest for the first time, often notice unusual bright or dark features when displaying one of the many possible polarization representations of the data (e.g., total power, HH, VV, or HV cross section, synthesized cross sections for arbitrary transmit and received polarizations, HH-VV phase difference, HH-VV correlation coefficient, etc.)

It is usually pertinent to ask what scattering mechanisms give rise to the observed features.

Much excellent work (for example, [1]–[5]) has been done on modeling polarimetric radar backscatter for both naturally occurring terrain and man-made objects. These models are usually complex and require a large number of input parameters to successfully predict the observed backscatter. For example, in modeling the backscatter return from a forest, measurements of tree heights and diameters, tree density, leaf size and angular distribution, branch size and angular distribution, trunk dielectric constants, ground roughness, and dielectric constant are commonly required as inputs. All of these models solve the "forward problem" in predicting backscatter from a number of ground-based measurements of the imaged objects. It is difficult, if not impossible, to invert these models to provide a unique solution, simply because the number of input parameters (the "ground truth") is often much larger than the number of output parameters (the radar measurements) in the forward problem.

As understanding of polarimetric scattering mechanisms has advanced, some excellent publications have appeared in the literature that can be used to gain a better understanding of polarimetric SAR measurements. An early example can be found in Huynen's ground-breaking thesis [6]. Another good example is van Zyl's paper on classifying the dominant scattering mechanism for each pixel [7]. Decomposition of the target scattering matrix into three orthogonal components has been proposed by Cloude [8], Holm and Barnes [9], van Zyl [10], and Krogager [11]. Cloude and Pottier [12] have produced an excellent review of these decomposition theorems. A common limitation of these decompositions is that they tend to be mathematically based and may yield combinations of three scattering matrices that cannot be so easily related to physical scattering models. In some cases, the underlying physical bases for the scattering decompositions can be traced to man-made or "hard" targets, such as metallic spheres or dihedrals and trihedrals, which may not be representative of scattering occurring from natural targets, such as forests and other vegetated areas. There is also a tendency to require orthogonality between at least two of the scattering components, which may be overly restrictive for natural scatterers.

In this paper, a technique for fitting a physically based, three-component scattering mechanism model to the polarimetric SAR data itself, without utilizing any ground truth measurements, is presented in Section II. This model was previously developed in Freeman and Durden [14]. The three scattering mechanism components included in the model are
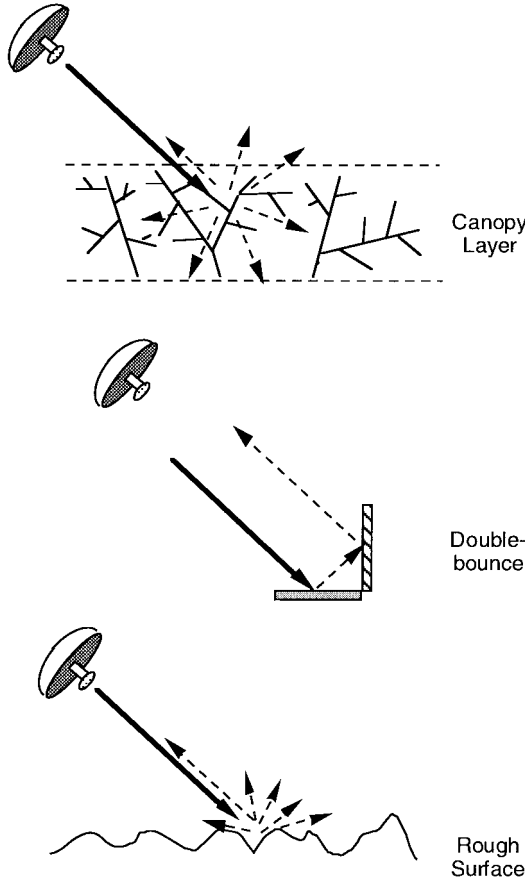
Fig. 1.   Sketch of the three scattering mechanisms used in the model: canopy scatter (top), surface scatter (middle), and double-bounce scatter (bottom).

canopy scatter from randomly oriented dipoles, first-order Bragg surface scatter, and a double-bounce scattering mechanism. The model fit yields an estimate of the contribution to the total backscatter of each of the three components. The backscatter contributions can also be compared to give the relative percentage weight of each, or used to estimate the contribution of each mechanism to the HH, HV, and VV backscatter terms. The model fit has an equal number of input parameters (the polarimetric radar backscatter measurements) and output parameters (the backscatter contributions from each of the three components and two parameters describing them). The model can be applied to entire images or to small areas within an image to give an estimate of the relevant scattering mechanisms. The model has been applied to many C-, L-, and P-band AIRSAR images of different types of terrain and to many C- and L-band SIR-C images. Results are presented for the model when applied to tropical rain forest data obtained from the NASA/JPL AIRSAR in Section III. These results are analyzed in more detail in Section IV, where it is also shown how the model can be used to predict changes in radar polarimetric signatures. Finally, the paper is summarized in Section V.

II. THE MODEL

The model fit includes three very simple scattering mechanisms, as illustrated in Fig. 1. First, for canopy (or volume) scattering, it is assumed that the radar return is from a cloud of randomly oriented, very thin, cylinder-like scatterers.

By making several simplifying assumptions, the second-order statistics of the resulting scattering matrix can be derived. First, let canopy scattering be represented by scattering from scatterers with the following scattering matrix when in standard orientation:

$$\mathbf{S} = \begin{pmatrix} S_v & 0 \\ 0 & S_h \end{pmatrix}. \tag{1}$$

We then assume that the scatterers are randomly oriented about the radar look direction with an angle ϕ from the vertical polarization direction. For a particular scatterer, the scattering matrix can be found by rotating into a coordinate system with vertical along the scatterer's standard orientation. We then calculate the scattered field and rotate back to the radar coordinate system. The following equation gives the scattering matrix in the radar coordinate system in terms of the scattering matrix in the scatterer's coordinate system:

$$\begin{pmatrix} S_{vv} & S_{vh} \\ S_{hv} & S_{hh} \end{pmatrix} = \begin{pmatrix} \cos\phi & \sin\phi \\ -\sin\phi & \cos\phi \end{pmatrix} \mathbf{S} \begin{pmatrix} \cos\phi & -\sin\phi \\ \sin\phi & \cos\phi \end{pmatrix}. \tag{2}$$

On multiplying the matrices in this equation, we find the following scattering matrix:

$$\begin{pmatrix} S_{vv} & S_{vh} \\ S_{hv} & S_{hh} \end{pmatrix}$$
$$= \begin{pmatrix} S_h \sin^2\phi + S_v \cos^2\phi & (S_v - S_h)\cos\phi\sin\phi \\ (S_v - S_h)\cos\phi\sin\phi & S_h \cos^2\phi + S_v \sin^2\phi \end{pmatrix}. \tag{3}$$

Note that the radar transmit and receive coordinate systems are identical, resulting in a symmetric scattering matrix, with $S_{hv} = S_{vh}$. The probability density function (pdf) for scatterer orientation is $p(\phi)$, and the expected value of any function $f(\phi)$ is

$$\langle f \rangle = \int_0^{2\pi} d\phi \, f(\phi) p(\phi). \tag{4}$$

The following are expressions for the second-order scattering matrix statistics (alternately, the covariance matrix statistics):

$$\langle |S_{vv}|^2 \rangle = a_1 |S_v|^2 + 2a_2 \operatorname{Re}(S_h S_v^*) + a_3 |S_h|^2$$
$$\langle |S_{hh}|^2 \rangle = a_1 |S_h|^2 + 2a_2 \operatorname{Re}(S_h S_v^*) + a_3 |S_v|^2$$
$$\langle |S_{hv}|^2 \rangle = a_2 |S_v|^2 - 2a_2 \operatorname{Re}(S_h S_v^*) + a_2 |S_h|^2$$
$$\langle S_{hh} S_{vv}^* \rangle = (a_1 + a_3) \operatorname{Re}(S_h S_v^*) + a_2 (|S_h|^2 + |S_v|^2) \tag{5}$$
$$\qquad\qquad + i(a_1 - a_3) \operatorname{Im}(S_h S_v^*)$$
$$\langle S_{hh} S_{hv}^* \rangle = a_4 (S_h S_v^* - |S_h|^2) + a_5 (|S_v|^2 - S_v S_h^*)$$
$$\langle S_{hv} S_{vv}^* \rangle = a_4 (|S_v|^2 - S_h S_v^*) + a_5 (S_v S_h^* - |S_h|^2)$$

where

$$a_1 \equiv \int_0^{2\pi} d\phi \cos^4\phi \, p(\phi)$$

$$a_2 \equiv \int_0^{2\pi} d\phi \cos^2\phi \sin^2\phi \, p(\phi)$$

$$a_3 \equiv \int_0^{2\pi} d\phi \sin^4\phi \, p(\phi)$$

$$a_4 \equiv \int_0^{2\pi} d\phi \cos^3\phi \sin\phi \, p(\phi)$$

and

$$a_5 \equiv \int_0^{2\pi} d\phi \cos\phi \sin^3\phi \, p(\phi).$$

We further simplify by assuming thin cylindrical scatterers so that S_v equals one and S_h equals zero. Furthermore, we assume a uniform orientation distribution $p(\phi)$, which gives $a_1 = a_3 = 3\pi/4, a_2 = \pi/4$, and $a_4 = a_5 = 0$. In this case, taking out a factor of π, we have, for the canopy (or volume) scatter

$$\langle |S_{\text{hh}}|^2 \rangle = \langle |S_{\text{vv}}|^2 \rangle = 1$$
$$\langle S_{\text{hh}} S_{\text{vv}}^* \rangle = \langle |S_{\text{hv}}|^2 \rangle = 1/3 \qquad (6)$$

and

$$\langle S_{\text{hh}} S_{\text{hv}}^* \rangle = \langle S_{\text{hv}} S_{\text{vv}}^* \rangle = 0.$$

The double-bounce scattering component is modeled by scattering from a dihedral corner reflector, where the reflector surfaces can be made of different dielectric materials, corresponding to a ground-trunk interaction for forests, for example. The vertical surface (e.g., the trunk) has reflection coefficients R_{th} and R_{tv} for horizontal and vertical polarizations, respectively. The horizontal surface (the ground) has Fresnel reflection coefficients R_{gh} and R_{gv}. The model can be made more general by incorporating propagation factors $e^{j2\gamma_v}$ and $e^{j2\gamma_h}$, where the γ are complex, which represent any attenuation and phase change of the vertically and horizontally polarized waves as they propagate from the radar to the ground and back again. In this way, the model can include the effects of propagation through a canopy layer or a trunk layer. The scattering matrix for double-bounce scattering is then

$$\mathbf{S} = \begin{bmatrix} e^{j2\gamma_v} R_{\text{gv}} R_{\text{tv}} & 0 \\ 0 & e^{j2\gamma_h} R_{\text{gh}} R_{\text{th}} \end{bmatrix}. \qquad (7)$$

The second-order statistics for double-bounce scattering, after normalization, with respect to the VV term, are

$$\langle |S_{\text{hh}}|^2 \rangle = |\alpha|^2, \quad \langle |S_{\text{vv}}|^2 \rangle = 1$$
$$\langle S_{\text{hh}} S_{\text{vv}}^* \rangle = \alpha, \quad \langle |S_{\text{hv}}|^2 \rangle = 0$$

and

$$\langle S_{\text{hh}} S_{\text{hv}}^* \rangle = \langle S_{\text{hv}} S_{\text{vv}}^* \rangle = 0$$

where

$$\alpha = e^{j2(\gamma_h - \gamma_v)}(R_{\text{gh}} R_{\text{th}}/R_{\text{gv}} R_{\text{tv}}). \qquad (8)$$

Two key features of this model for double-bounce (or even-bounce) scatter are that the amplitudes of the HH and VV terms do not have to be equal and the phase difference between the HH and VV terms (i.e., $\arg(S_{\text{hh}} S_{\text{vv}}^*)$ or $\arg(\alpha)$) does not have to be $\pm\pi$. It will be shown later that this is necessary to match the observed behavior of scattering from many natural targets.

For the surface scatter, a first-order Bragg model is used with second-order statistics (after normalization)

$$\langle |S_{\text{hh}}|^2 \rangle = |\beta|^2, \quad \langle |S_{\text{vv}}|^2 \rangle = 1$$
$$\langle S_{\text{hh}} S_{\text{vv}}^* \rangle = \beta, \quad \langle |S_{\text{hv}}|^2 \rangle = 0$$

and

$$\langle S_{\text{hh}} S_{\text{hv}}^* \rangle = \langle S_{\text{hv}} S_{\text{vv}}^* \rangle = 0 \qquad (9)$$

where β is real. For all of these backscatter components, it is assumed that the backscatter is reciprocal. It has also been

shown that the like- and cross-polarized returns are uncorrelated. Further, assuming that the volume, double-bounce, and surface scatter components are uncorrelated, the total second-order statistics are the sum of the above statistics for the individual mechanisms. Thus, the model for the total backscatter is

$$\langle |S_{\text{hh}}|^2 \rangle = f_s |\beta|^2 + f_d |\alpha|^2 + f_v$$
$$\langle |S_{\text{vv}}|^2 \rangle = f_s + f_d + f_v$$
$$\langle S_{\text{hh}} S_{\text{vv}}^* \rangle = f_s \beta + f_d \alpha + f_v/3$$
$$\langle |S_{\text{hv}}|^2 \rangle = f_v/3$$

and

$$\langle S_{\text{hh}} S_{\text{hv}}^* \rangle = \langle S_{\text{hv}} S_{\text{vv}}^* \rangle = 0 \qquad (10)$$

where f_s, f_d, and f_v are the surface, double-bounce, and volume (or canopy) scatter contributions to the VV cross section. If f_s, f_d, and f_v can be estimated, it follows from (10) that the contributions of surface, double-bounce, and volume scatter to the HH, HV, and VV backscatter can be readily separated.

This model gives us four equations in five unknowns (ignoring the cross products between like and cross pol). In general, a solution can be found if one of the unknowns is fixed. Since neither the surface or double-bounce mechanisms contribute to the HV term in the model, we can use this to estimate the volume scatter contribution directly. The volume contribution f_v or $f_v/3$ can then be subtracted off the $|S_{\text{HH}}|^2$, $|S_{\text{VV}}|^2$, and $S_{\text{HH}} S_{\text{VV}}^*$ terms, leaving three equations in four unknowns

$$\langle |S_{\text{hh}}|^2 \rangle = f_s |\beta|^2 + f_d |\alpha|^2$$
$$\langle |S_{\text{vv}}|^2 \rangle = f_s + f_d \qquad (11)$$
$$\langle S_{\text{hh}} S_{\text{vv}}^* \rangle = f_s \beta + f_d \alpha.$$

After van Zyl [7], we then decide whether double-bounce or surface scatter is the dominant contribution in the residual, based on the sign of the real part of $S_{\text{hh}} S_{\text{vv}}^*$. If $\text{Re}(S_{\text{hh}} S_{\text{vv}}^*)$ is positive, we decide that surface scatter is dominant and fix $a = -1$. If $\text{Re}(S_{\text{hh}} S_{\text{vv}}^*)$ is negative, we decide that double-bounce scatter is dominant in the remainder and fix $\beta = 1$. Then f_s, f_d, and β or α can be estimated from the residual radar measurements. This approach will obviously work best when either f_s or f_d are close to zero, or when α or β are close to -1 or $+1$.

Finally, we estimate the contribution of each scattering mechanism to the span P

$$P = P_s + P_d + P_v \equiv \left(|S_{\text{hh}}|^2 + 2|S_{\text{hv}}|^2 + |S_{\text{vv}}|^2 \right)$$

with

$$P_s = f_s(1 + |\beta|^2)$$
$$P_d = f_d(1 + |\alpha|^2)$$

and

$$P_v = 8f_v/3. \qquad (12)$$

Note that P is just four times the usual expression for total power.

KEY:

- Upland forest
- Bajo
- Escarpment
- Farmland
- Bare soil
- Regrowth
- Clear-cut
- Coffee
- Flooded forest
- Local village
- Laguna Verde (Water)
- Laguna Seca (Reeds)
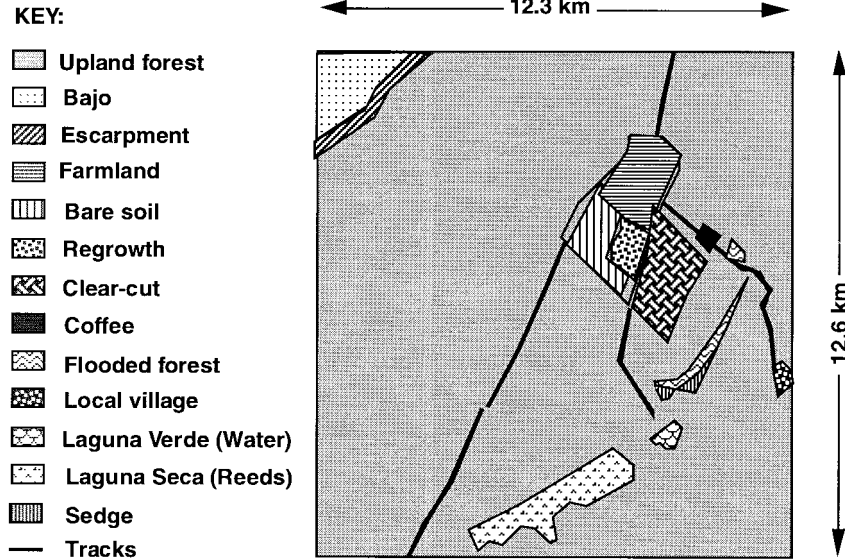- Sedge
- — Tracks

12.3 km

12.6 km

Fig. 2. Land cover map of the Gallon Jug area in northwest Belize.

III. RESULTS

In March 1990, NASA/JPL's airborne SAR system, known as AIRSAR, was flown over an area around Gallon Jug in Belize, which had been chosen for intensive field study. This intensive study area in northern Belize is dominated by old growth upland tropical rain forest. There are also small areas that have been cleared of upland forest within the last five years and allowed to regrow. In addition, there are areas of almost pure palm forest, consisting of either cohune or botan palm trees. There are several types of wetland forests. High marsh forest has vegetation resembling the upland rain forest, but standing water is present during a large portion of the year. Bajo is another type of wetland forest that grows in areas having very poorly drained clay soils. The vegetation is short (less than 10 m), densely packed, and has sparse foliage. Yet another wetland forest type is swamp forest, consisting of short trees or shrubs growing in standing water. Besides forest, there are reed and sedge marshes. These are areas of herbaceous vegetation in standing water. The sedges are considerably taller than reeds (200 versus 40 cm). In addition to these naturally occurring vegetation types, there are agricultural areas, consisting of cleared areas, bare soil, and various crops. A map of land cover for the area is given in Fig. 2, based on *in-situ* measurements and on aerial overflights of the Gallon Jug area.

Three-frequency, multipolarization, AIRSAR data of the area were calibrated using corner reflectors deployed in clearings near Gallon Jug. The Gallon Jug area is a large plantation surrounded by rain forest. Fig. 3 shows the result of applying the model described in Section II to this data. In the figure, the contributions of each of the three scattering mechanisms to the total power are shown for each pixel, with surface scatter colored blue, volume scatter green, and double-bounce red. Results are shown for all three AIRSAR frequencies (C-, L-, and P-band, corresponding to 6-, 24-, and 68-cm wavelengths, respectively). The relative strength of each color

in the resulting Red-Green-Blue (RGB) images can be related to the relative strengths of the scattering mechanisms. The AIRSAR viewing direction is from the top of each frame.

Tables I–III show typical backscatter values for representative samples for the land cover types in the Gallon Jug area, together with quantitative estimates for the contributions to the total backscatter for each of the three scattering mechanisms $(P_s, P_d,$ and $P_v)$. Average values are given in each table for the incidence angle θ_i, the span P, the HH backscatter (σ^o_{hh}), the ratio of VV to HH backscatter $(\sigma^o_{vv}/\sigma^o_{hh})$, the ratio of HV to HH backscatter $(\sigma^o_{hv}/\sigma^o_{hh})$, the phase difference between the HH and VV measurements ϕ^*_{hhvv} $(= \arg(S_{hh}S^*_{vv}))$, and the correlation between the HH and VV measurements ρ^*_{hhvv}. Note that no results are presented here for the $S_{hh}S^*_{hv}$ or $S_{hv}S^*_{vv}$ terms. This is because the results were all close to zero, except in the case of the reeds and sedge areas. The reason for the nonzero values obtained for the like- to cross-pol cross products for these two cases will be the subject of future paper.

Results for land cover types marked with an asterisk were obtained from AIRSAR images of scenes adjacent to the one depicted in Fig. 3 in the Gallon Jug area and are presented here because they represent some unusual features. The sample results are arranged in each table according to the strength of the observed P-band HH backscatter. Recent results linking this parameter to biomass (e.g., [15] and [16]) indicate that the sample results are approximately ranked in order of increasing biomass. Note that the expected noise floor for each polarization is between -25 and -30 dB for the C-band AIRSAR data and between -35 and -40 dB for the L- and P-band AIRSAR data. The noise floor for the span P should be 6 dB above these levels. Estimated backscatter contributions within or below these ranges should be considered negligible.

The results given in Fig. 3 and Tables I–III show that the model fits the scattering behavior for bare soil quite well at P-band, with surface scatter being by far the strongest component. At L- and C-band, surface scatter is still dominant
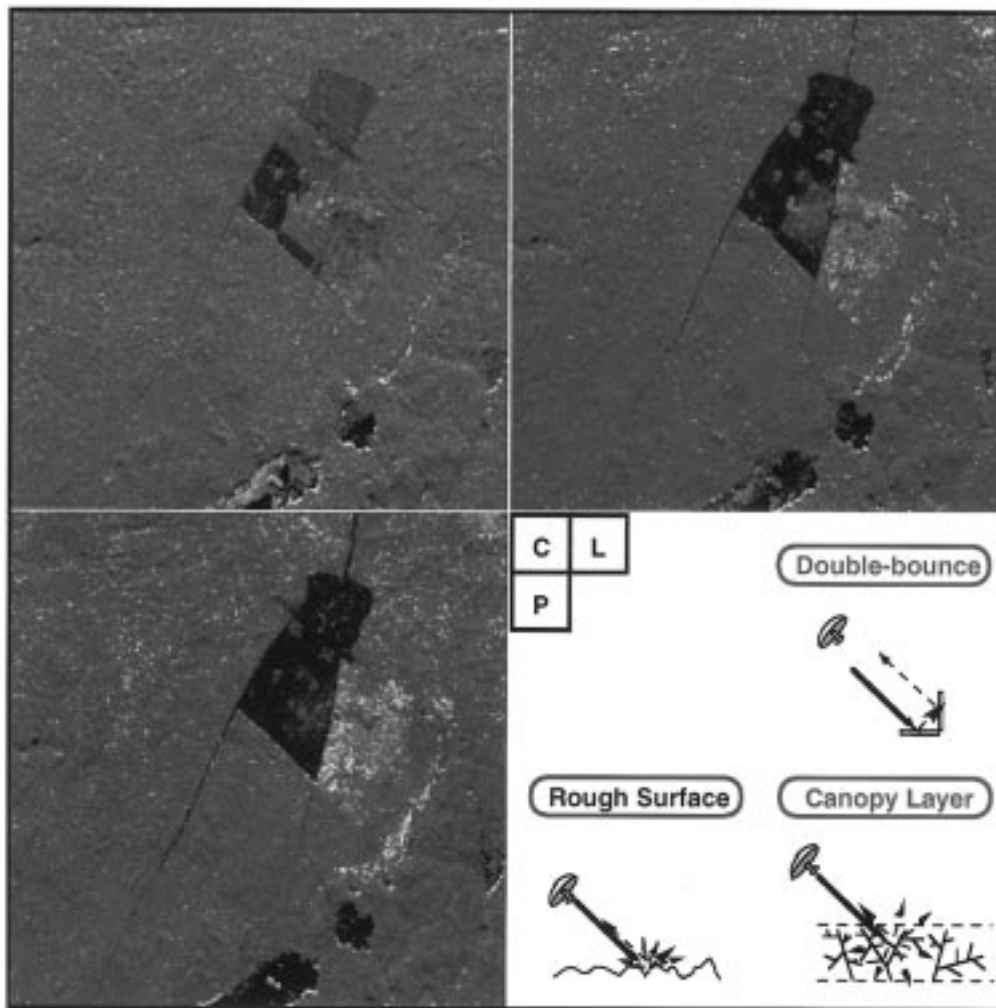
Fig. 3. Application of the model to a three-frequency, multipolarization AIRSAR data set over the Gallon Jug area, showing the scattering mechanism contributions overlaid in color for each frequency band (P-, L-, and C-band).

for bare soil, but a significant amount of volume scatter is present. This indicates that perhaps the small perturbation model used for surface scatter is not completely valid for the surface/wavelength in these cases, since it does not allow any depolarization due to surface scatter. For open water, the small perturbation model fits quite well at all three frequencies, except for a "volume scatter" component, which comes from an HV measurement that is close to the level of the noise floor for each channel.

Farmland has volume scatter dominant at C-band, but surface scatter dominant at L- and P-band. This can be interpreted as indicating that the longer wavelengths are penetrating the relatively short vegetation in the farmland area and the backscatter is mostly from the underlying ground.

The model for volume or canopy scatter fits the observations for Upland Forest at L-band very well, with only a small amount of double-bounce resulting from the model fit. At C-band, the model works quite well for Upland Forest, except for the presence of a significant surface scatter term, in addition to the dominant volume scatter term. The double-bounce term is very small. In fact, this mix of a dominant volume scatter term with a lesser surface scatter term is characteristic of all

the forest classes at C-band in the Belize data. At P-band, the Upland Forest has volume or canopy scatter dominant, with a now significant level of double-bounce, which is 6.4 dB less than (or a factor of 0.23, which is just over one-fifth) the volume scatter term. This is to be expected, given the increased ability at longer wavelengths to penetrate vegetation canopies, which has been noted in several studies, e.g., [17].

Forest areas that show significantly increased levels of double-bounce relative to volume scatter at P-band (when compared with the Upland Forest) are Bajo, Swamp Forest, Palm Forest, Flooded Forest, and the Coffee Plantation. These areas can be characterized as having either a lower canopy height than the Upland Forest, a sparser canopy, a wetter ground surface, or some combination of the three. The same areas, with the exception of the flooded forest, exhibit an increased level of double-bounce relative to volume scatter at L-band, but to a lesser degree. There is a significant increase in the double-bounce term for the Swamp forest and High Marsh Forest at C-band.

Regrowth is clearly separable from Upland Forest at P-band since the level of canopy scatter is significantly lower (-12.1 compared to -8.8 dB). This result stems from the difference

TABLE I
AVERAGE P-BAND BACKSCATTER VALUES AND ESTIMATED SCATTERING MECHANISM
CONTRIBUTIONS FOR DIFFERENT LAND COVER TYPES FROM AIRSAR BELIZE DATA

P-BAND	θ_i	P	σ^0_{hh}	VV/HH	HV/HH	$\phi hhvv^*$	$\rho hhvv^*$	P_s	P_d	P_v
	(deg.)	(dB)	(dB)	(dB)	(dB)	(deg.)		(dB)	(dB)	(dB)
Open water	54.1	-24.8	-32.6	6.6	-7.4	5.8	0.33	-26.6	-35.3	-31.0
Bare soil	46.6	-18.4	-25.1	5.4	-9.5	-8.8	0.75	-19.6	-33.6	-25.4
Reeds	56.2	-16.7	-22.0	3.3	-8.6	146.7	0.27	-32.0	-25.3	-27.6
Farmland	34.9	-15.9	-20.3	2.0	-11.5	-12.5	0.53	-17.8	-23.9	-23.1
Regrowth	44.8	-10.9	-15.3	0.9	-5.8	20.7	0.25	-19.4	-21.4	-12.1
Bajo*	45.1	-9.2	-14.5	2.8	-5.8	70.8	0.21	-19.1	-15.0	-11.1
Swamp forest*	47.8	-9.9	-13.8	0.6	-8.4	149.5	0.10	-17.9	-14.2	-13.2
Upland Forest	40.0	-7.7	-11.5	-0.4	-6.4	51.1	0.14	-20.7	-15.2	-8.8
Palm Forest*	36.7	-7.6	-11.3	0.1	-7.2	91.4	0.21	-24.5	-11.6	-9.8
Sedge	44.2	-6.7	-10.3	-0.5	-7.0	93.6	0.18	-18.2	-12.7	-8.3
Flooded Forest	51.9	-6.3	-9.7	-0.9	-7.0	75.6	0.16	-19.3	-13.0	-7.6
Coffee	43.1	-6.2	-9.2	-1.3	-8.8	137.3	0.40	-90.0	-9.5	-8.8
Clear-cut	46.0	-6.5	-9.0	-3.0	-8.5	31.0	0.32	-11.7	-18.0	-8.5
High Marsh Forest*	29.1	-3.8	-8.2	1.6	-7.5	-32.7	0.29	-9.0	-11.0	-6.7

TABLE II
AVERAGE L-BAND BACKSCATTER VALUES AND ESTIMATED SCATTERING MECHANISM
CONTRIBUTIONS FOR DIFFERENT LAND COVER TYPES FROM AIRSAR BELIZE DATA

L-BAND	θ_i	P	σ^0_{hh}	VV/HH	HV/HH	$\phi hhvv^*$	$\rho hhvv^*$	P_s	P_d	P_v
	(deg.)	(dB)	(dB)	(dB)	(dB)	(deg.)		(dB)	(dB)	(dB)
Open water	54.1	-20.1	-28.7	7.7	-6.6	-3.1	0.63	-21.3	-40.1	-26.5
Bare soil	46.6	-12.2	-16.5	1.8	-10.4	-23.7	0.75	-14.1	-23.7	-17.9
Reeds	56.2	-8.5	-12.9	1.6	-7.5	131.4	0.13	-23.7	-18.8	-17.4
Farmland	34.9	-9.3	-13.3	1.5	-11.7	-18.6	0.75	-10.9	-20.2	-15.7
Regrowth	44.8	-6.0	-10.1	0.1	-5.5	-22.7	0.31	-16.9	-18.9	-6.5
Bajo*	45.1	-5.7	-9.7	-0.1	-5.6	15.1	0.17	-22.7	-15.3	-6.3
Swamp forest*	47.8	-3.4	-6.9	-0.4	-7.6	165.4	0.06	-13.8	-8.7	-5.4
Upland Forest	40.0	-5.1	-9.2	-0.2	-5.1	7.9	0.25	-90.0	-18.1	-5.3
Palm Forest*	36.7	-5.0	-8.6	-0.6	-6.4	48.5	0.20	-15.9	-13.5	-6.0
Sedge	44.2	-4.6	-8.8	0.2	-5.2	-5.7	0.26	-21.5	-16.8	-5.0
Flooded Forest	51.9	-4.8	-8.6	-0.6	-5.6	31.4	0.22	-90.0	-90.0	-5.1
Coffee	43.1	-5.0	-8.0	-1.7	-7.7	52.1	0.12	-16.5	-11.0	-6.6
Clear-cut	46.0	-4.8	-7.6	-2.0	-8.0	6.9	0.40	-10.1	-17.0	-6.6
High Marsh Forest*	29.1	-1.1	-4.0	-2.1	-7.8	-2.5	0.32	-7.3	-12.7	-2.7

TABLE III
AVERAGE C-BAND BACKSCATTER VALUES AND ESTIMATED SCATTERING MECHANISM
CONTRIBUTIONS FOR DIFFERENT LAND COVER TYPES FROM AIRSAR BELIZE DATA

C-BAND	θ_i	P	σ^0_{hh}	VV/HH	HV/HH	$\phi hhvv^*$	$\rho hhvv^*$	P_s	P_d	P_v
	(deg.)	(dB)	(dB)	(dB)	(dB)	(deg.)		(dB)	(dB)	(dB)
Open water	54.1	-18.5	-23.7	2.4	-5.3	-18.7	0.29	-24.7	-31.5	-20.0
Bare soil	46.6	-5.4	-9.0	0.3	-8.9	-10.0	0.76	-7.9	-25.4	-8.9
Reeds	56.2	-2.2	-5.2	-1.3	-8.7	102.5	0.16	-17.4	-12.7	-10.9
Farmland	34.9	-4.0	-7.6	-0.7	-6.4	-1.2	0.47	-10.9	-24.0	-5.0
Regrowth	44.8	-2.0	-5.7	-0.7	-6.5	3.2	0.44	-9.2	-19.0	-3.1
Bajo*	45.1	-2.1	-6.2	0.2	-5.6	-2.1	0.42	-10.6	-22.0	-2.7
Swamp forest*	47.8	0.9	-2.1	-1.2	-8.9	2.3	0.41	-3.5	-8.3	-1.9
Upland Forest	40.0	-2.0	-5.6	-0.6	-6.6	-4.1	0.51	-8.4	-22.0	-3.2
Palm Forest*	36.7	-1.3	-5.0	-0.4	-7.0	-2.4	0.56	-6.7	-21.3	-2.9
Sedge	44.2	-2.3	-6.1	0.0	-6.3	-0.9	0.52	-8.4	-22.2	-3.5
Flooded Forest	51.9	-2.0	-6.4	0.9	-5.5	-2.3	0.42	-9.7	-19.0	-2.9
Coffee	43.1	-3.3	-6.6	-1.4	-7.0	6.9	0.42	-9.7	-17.3	-4.6
Clear-cut	46.0	-2.9	-6.0	-1.4	-8.3	8.3	0.55	-7.2	-16.9	-5.2
High Marsh Forest*	29.1	0.0	-3.2	-1.5	-7.0	15.0	0.35	-7.2	-13.0	-1.2

in the level of HV backscatter for these two classes, which can be interpreted as a difference in the level of biomass, with the Regrowth being lower. At L-band, the level of canopy scatter is only slightly lower (by 1 dB) for the Regrowth, which cannot be regarded as significant. However, it may be possible to differentiate between the Upland Forest and the Regrowth based on the presence of an increased level of surface scatter for the Regrowth. At C-band, the Regrowth and Upland Forest results are virtually identical.

Sedge is indistinguishable from Upland Forest at C-band, but exhibits an increased level of double-bounce (relative to canopy scatter) at L- and P-band. Reeds have a relatively large fraction of double-bounce at each frequency, but only at C-band is the overall level of the backscatter very high ($P = -8.2$ dB). Both Reeds and Sedge can be characterized as a collection of cylindrical objects over a water surface. The major difference between the two is in vegetation height and therefore biomass. Thus, an interpretation of the results is that the Reeds have enough biomass to give a significant level of volume and double-bounce scatter at C-band, but not at L- and P-band. At all three frequencies, a large proportion of the backscatter for the Reeds comes from the double-bounce
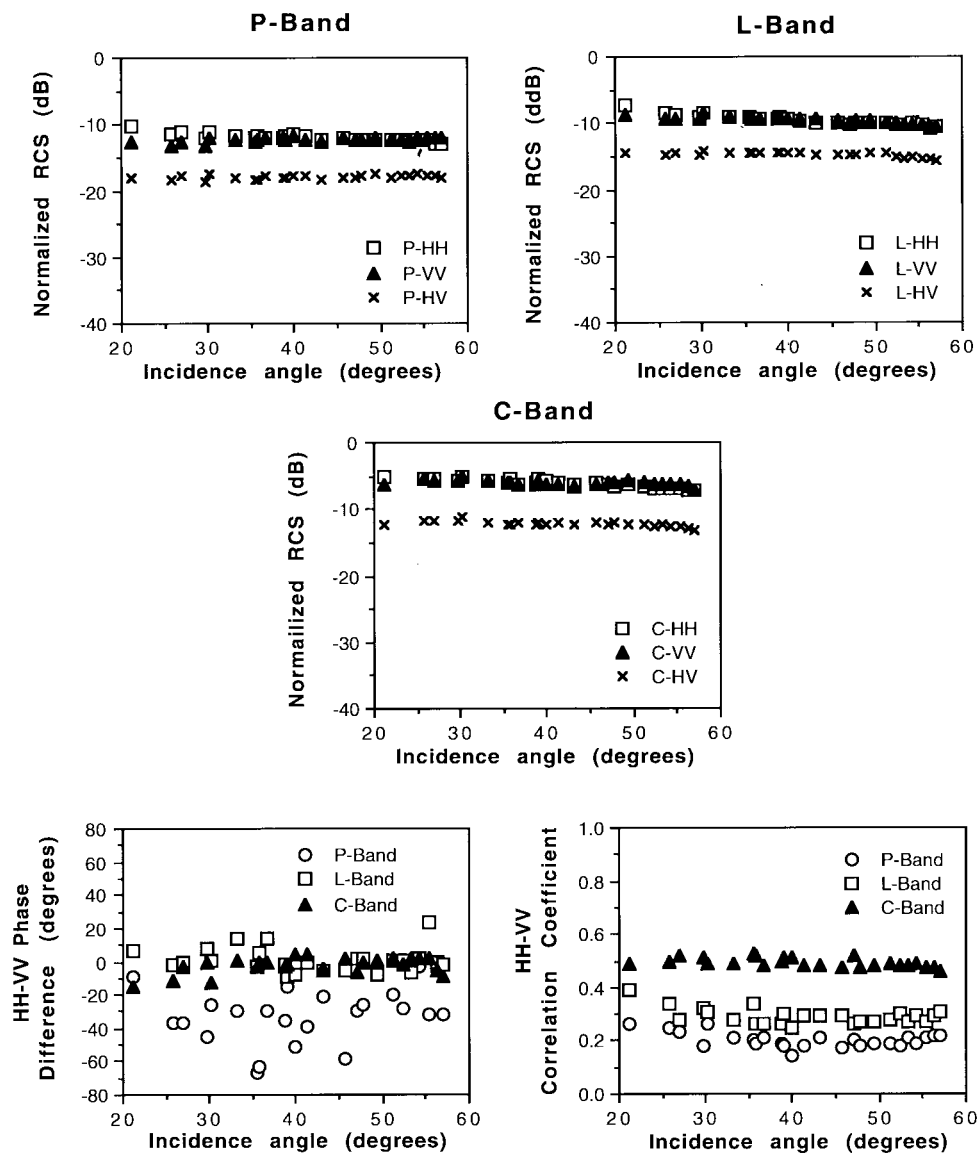
Fig. 4. Backscatter measurements over the three frequency bands versus incidence angle for Upland Forest from the Gallon Jug AIRSAR data set.

interaction between the cylinders and the water surface. For the Sedge, the canopy layer is too thick for the C-band to penetrate, so there is no significant double-bounce term at that wavelength.

The clear-cut area in the Gallon Jug scene is rather unusual, in that at the time of the data collection, the area had been recently bulldozed and the fallen tree trunks and branches were lying on the ground prior to burning. The scattering mechanism results indicate that there is an increased level of surface scatter for this area at all three frequencies, but especially at L- and P-band. This can be interpreted as an increase in the level of the direct return from the tree-trunks lying horizontally on the ground in this area.

In Tables I–III, we have only presented results for the Upland Forest at one incidence angle (40°). In Fig. 4, we show the backscatter measurements for Upland Forest over a range of incidence angles between 21 and 58°. The VV and HV backscatter values are fairly uniform across the range of incidence angles for L- and P-band, while the HH results

show a tendency to increase at smaller incidence angles. At C-band, all three polarizations show the same slightly downward trend with increasing incidence angle. The phase difference between HH and VV shows some variability at L- and P-band, and is mostly zero at C-band, except at smaller incidence angles. The correlation between the two like-pol measurements is fairly constant across incidence angles at C-band, but shows a slight but significant increase at smaller incidence angles at L- and P-band. In Fig. 5, we show the estimated backscatter measurements for each frequency, again versus incidence angle. These results show a marked increase in the surface scatter term at L- and P-band at smaller incidence angles. This can be interpreted as an increase in the direct return from the ground. The results also show a decrease in the double-bounce term at P-band outside the range of incidence angles between 30 and 50°. The C-band results are fairly consistent across the full range of incidence angles. Note that the C-band double-bounce results are mainly close to the noise floor for that frequency. The slight rise in the double-bounce term at smaller
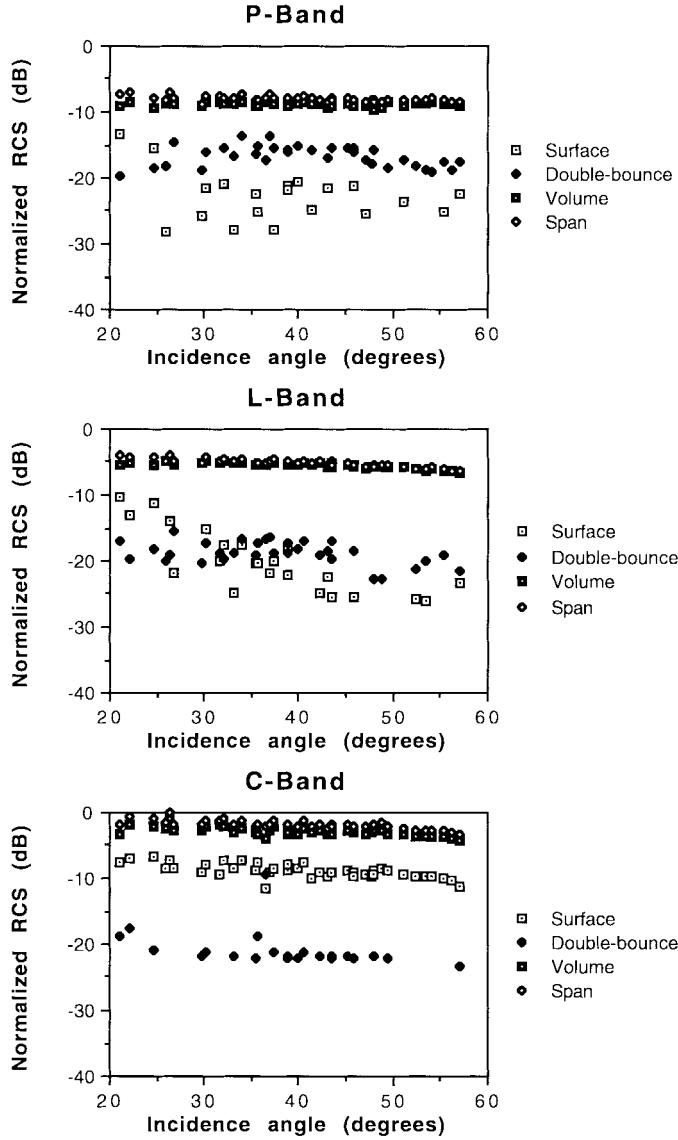
Fig. 5. Estimated scattering mechanism contributions over the three frequency bands versus incidence angle for Upland Forest from the Gallon Jug data set.
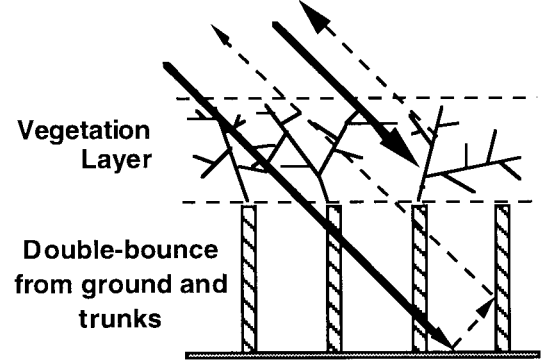
Fig. 6. Two-component scattering from Upland Forest showing the main contributors as vegetation layer scattering and double-bounce from the ground-trunk interaction.

incidence angles may (or may not) be significant, depending on the behavior of the noise floor in that part of the data.

IV. FURTHER ANALYSIS

The results presented in Section III for P-band AIRSAR data over the Gallon Jug area indicate that surface scattering is not an important contribution for Upland Forest for incidence angles greater than 30°. So the backscatter for Upland Forest at P-band in this range is well described by a two-component version of our model, as depicted in Fig. 6, with $f_s = 0$ in (10), i.e.,

$$\langle |S_{hh}|^2 \rangle = f_d |\alpha|^2 + f_v$$
$$\langle |S_{vv}|^2 \rangle = f_d + f_v$$
$$\langle S_{hh} S_{vv}^* \rangle = f_d \alpha^2 + f_v/3$$
$$\langle |S_{hv}|^2 \rangle = f_v/3$$

and

$$\langle S_{hh} S_{hv}^* \rangle = \langle S_{hv} S_{vv}^* \rangle = 0. \tag{13}$$

Recall from (8) that α represents the relative amplitude and phase difference between the HH and VV backscatter for double bounce and is given by the product of a term that represents propagation through the canopy and the ratio of the HH and VV reflection terms for the ground-trunk interaction. The canopy propagation term can be separated into two terms, one representing propagation through the canopy layer and the other, a layer consisting only of trunks, as depicted in Fig. 6. The reflection terms for the ground and trunk can also be separated into two terms, so that α can be written as

$$\alpha = \left[e^{j2(\gamma_h - \gamma_v)} \right]_{\text{canopy}} \left[e^{j2(\gamma_h - \gamma_v)} \right]_{\text{trunk}}$$
$$\cdot (R_{gh}/R_{gv})(R_{th}/R_{tv}). \tag{14}$$

It is possible, after [18], to calculate the reflection coefficients for the ground and trunk, if the dielectric constants of the two, the trunk radius and the incidence angle, are known. Adopting values from Table IV for the trunk dielectric constant of $40 - 20i$ [19], for the ground dielectric constant of $4 - 0.5i$ (representing dry soil, after [20]), a trunk radius of 0.1 m, and an incidence angle of 40°, we obtain

$$|R_{gh}| \simeq 1.8 |R_{gv}| \quad \text{and} \quad \arg(R_{gh}/R_{gv}) \simeq 0.$$

Note that the reflection coefficient for the H-component is larger than that for the V-component, as noted by others. For the trunk term, we obtain

$$|R_{th}| \simeq 1.3 |R_{tv}| \quad \text{and} \quad \arg(R_{th}/R_{tv}) \simeq 135.8. \tag{15}$$

Our calculations show that, for a randomly oriented canopy, the expected value of the H and V propagation terms are such that

$$\langle \gamma_h \rangle \text{canopy} = \langle \gamma_v \rangle \text{canopy}$$

which leaves only the propagation through the "trunk layer," as proposed by Ulaby *et al.* [16], which results in a change in

TABLE IV
UPLAND FOREST PARAMETERS USED IN PREDICTING THE DOUBLE-BOUNCE
SCATTER CHARACTERISTICS FOR THE P-BAND GALLON JUG DATA

Wavelength, λ	0.68 m
Incidence angle, θ	40 degrees
Trunk radius, a	0.1 m
Total canopy height	25 m
Height of trunk layer, h	15 m
Number density, N	0.1 (m^{-2})
Trunk dielectric constant, ε	40 - 20i
Ground dielectric constant, ε	4 - 0.5i

the phase of α due to propagation of

$$\arg\left\{e^{j2(\gamma_h - \gamma_v)}\right\}_{\text{trunk}} = \frac{4Nh\tan\theta}{k} \cdot [\text{Im}\{T_h(\theta,\pi)\} - \text{Im}\{T_v(\theta,\pi)\}]$$

(16)

where N is the number density of the trunk layer, h is the height of the trunk layer, k is the wavenumber, and the T_h and T_v terms represent the forward scattered field at each polarization for a single cylinder.

For the Belize data, from Table IV, the Upland Forest is $\sim$25-m high, with a trunk layer $\sim$15 m in height, and the number density of the trunks is $\sim$0.1. At P-band, for an incidence angle of 40°, we calculate

$$\arg\{e^{j(\gamma_h - \gamma_v)}\} \simeq 26.1.$$

Thus

$$\arg(\alpha) \simeq 161.9.$$

Returning to (13), we can predict some characteristics of the scattering behavior at P-band for Upland Forest at 40°, as a function of the relative contribution of the double-bounce and volume scatter, i.e., as a function of (P_d/P_v). This is shown in Fig. 7. On the left-hand side of each figure, the volume scatter term is dominant and the scattering behavior matches that described by (6). On the right-hand side, double-bounce scatter is dominant and the scattering behavior matches that described by (8). As the relative level of the double-bounce term increases, going from left to right, the phase difference increases. Note that between $P_d/P_v = 0.1$ and one, the phase difference can take any value in the range 10 to 160°. Initially, the correlation coefficient decreases as P_d/P_v increases from 0.33 to around 0.08 at $P_d/P_v = 0.35$. Thereafter, the correlation coefficient increases toward a value of one for double-bounce completely dominant. The values of HV/HH decreases steadily as the double-bounce term increases in significance, while the HH/VV term increases toward its value for double-bounce completely dominant. The general trends shown in Fig. 7 are consistent with our observations of polarimetric backscatter at L- and P-band for many different forest areas, for which the phase difference is usually somewhere between 0 and 180° (but often considerably less than 180°), the correlation coefficient is typically low (less than 0.5), the HV/HH ratio less than −5 dB, and the HH/VV ratio is equal to or slightly higher than 0 dB.
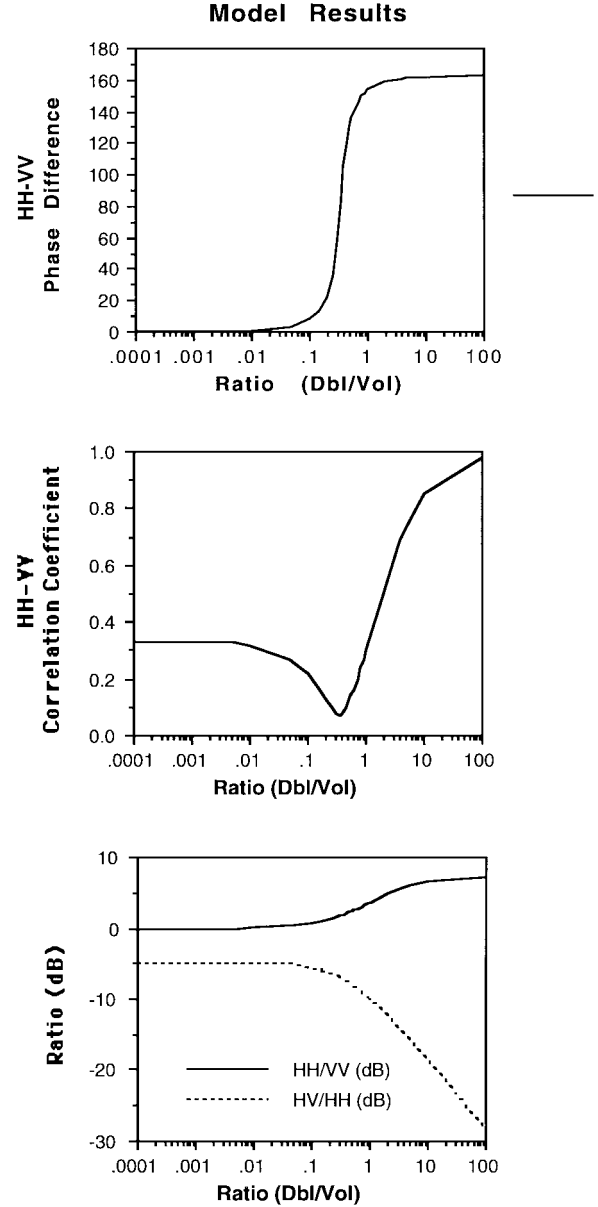

Fig. 7. Model predictions for backscatter characteristics as a function of the ratio of double-bounce to volume scatter (P_d/P_v) at P-band for Upland Forest at an incidence angle of 40°.

The model presented in this paper does not attempt to predict the absolute level of any backscatter measurement. Note, however, that the values on the charts for the HH-VV phase difference, the HH-VV correlation coefficient, and the ratios of HH/VV backscatter and HV/HH backscatter match very well with the results for Upland forest given in Table I, for a ratio of double-bounce to volume scatter of between 0.2 and 0.3, which is consistent with the observed ratio of 0.23. Matching the behavior of all four of these parameters at the same time is difficult; very few successful attempts to do so are documented in the literature.

Returning to (7), it is clear that, if the H and V Fresnel reflection coefficients for the forward scattering off the ground, i.e., R_{gh} and R_{gv}, increase, the strength of the double-bounce scattering term will increase. In general, this is precisely what

happens when inundation occurs, when the ground changes from soil or vegetation cover with a relatively low dielectric constant and forward reflection coefficient to water that has a relatively high dielectric constant and therefore a high reflection coefficient. (The dielectric constant for water at P-band is $80 - 2i$ compared with $4 - 0.5i$ for dry soil). To first order then, inundation produces an increase in the relative strength of the double-bounce scattering term compared to the volume or canopy scatter term. From Table I, we see that the flooded forest has 0.29 for the ratio of double-bounce to volume scatter at P-band, compared with 0.23 for the upland forest. We can see from Fig. 7 that an increase of this order in the relative strength of the double-bounce term will tend to increase the HH-VV phase difference and the HH/VV backscatter ratio. The HV/HH backscatter ratio will tend to decrease, and the HH-VV correlation coefficient will change only slightly. This broadly describes the behavior of the flooded forest results at P-band compared to the upland forest results in Table I.

The coffee plantation at the Gallon Jug site was selectively thinned, i.e., the owner of the Gallon Jug site removed many of the trees from that area of forest to grow a coffee crop beneath the shade of the remaining canopy. This means that the number density (N) of trunks in the coffee plantation and the attenuation through the canopy and the trunk layers (i.e., the γ_h and γ_v) were reduced in comparison to the nearby Upland Forest. Looking at (7) and (16), we see that the effects of this selective thinning will be to lower the HH-VV phase difference introduced by propagation through the trunk layer and to increase the strength of the double-bounce scattering term. Again, to first order, this change in the condition of the forest produces an increase in the relative strength of the double-bounce scattering term compared to the volume or canopy scatter term, assuming that the canopy is not thinned so much that the canopy scatter is significantly reduced. Comparing the coffee plantation results with the upland forest results in Table I, we see that there is a significant increase in the strength of the double-bounce term, but not the volume scatter term, so that the relative contribution of the double-bounce to the volume scatter increases from ~0.23 to ~0.85. From Fig. 7, we see that this trend should mean a significant increase in the HH-VV phase difference, HH-VV correlation coefficient, and HH/VV backscatter ratio. There should also be a corresponding decrease in the HV/HH backscatter ratio. This is confirmed by the results in Table I for P-band; similar behavior can be seen for the L-band results in Table II.

V. Summary and Discussion

A new technique for fitting simple backscatter mechanisms to polarimetric SAR data has been presented. This model-fitting approach has the advantage that it is based on the physics of radar scattering, not a purely mathematical construct. The model does not attempt to predict the absolute level of any backscatter measurement. It does match very well with the general polarimetric behavior of the scattering seen in a multifrequency, polarimetric data set obtained over a tropical rain forest site, containing a variety of land cover types.

The model-fitting approach worked well when fitted to the radar scattering from tropical rain forest over a wide range of incidence angles. The results showed a possible increase in the direct or surface scattering contribution at lower incidence angles at L- and P-band. The volume or canopy scatter term was relatively constant as a function of incidence angle. The double-bounce contribution at P-band showed a slight decrease for incidence angles either side of $40°$.

The model can be used to determine to first order what are the dominant scattering mechanisms that give rise to observed backscatter in polarimetric SAR data. We also showed how it can be used to predict, in a qualitative sense, the effects of certain changes, such as inundation and forest thinning, on the radar backscatter. Measurable changes due to these effects were seen at both L- and P-band in the fully polarimetric radar signature, the changes being more pronounced at P-band.

The three-component scattering mechanism model may prove useful in providing features for distinguishing between different surface cover types and in helping to determine the current state of that surface cover (e.g., flooded or nonflooded and frozen or thawed trees). In future work, we intend to use the scattering mechanism images as classification features to allow differentiation between different land cover types. We also intend to extend the scope of the model to include canopy scatterers with shapes other than dipoles, preferred orientation directions of scatterers, and tilted surfaces.

Acknowledgment

References

[1] S. L. Durden, J. J. van Zyl, and H. A. Zebker, "Modeling and observation of the radar polarization signature of forested areas," *IEEE Trans. Geosci. Remote Sensing*, vol. 27, pp. 290–301, May 1989.

[2] M. Moghaddam and S. Saatchi, "Analysis of scattering mechanisms in SAR imagery over boreal forest: Results from BOREAS'93," *IEEE Trans. Geosci. Remote Sensing*, vol. 33, pp. 1290–1295, Sept. 1995.

[3] S. L. Durden, J. D. Klein, and H. A. Zebker, "Polarimetric radar measurements of a forested area near Mt. Shasta," *IEEE Trans. Geosci. Remote Sensing*, vol. 29, pp. 444–450, May 1991.

[4] Y. Wang, "Radar backscatter modeling and applications in forested environments," Ph.D. dissertation, Univ. California, Santa Barbara, July 1992.

[5] F. T. Ulaby, K. Sarabandi, K. C. McDonald, M. Whitt, and M. C. Dobson, "Michigan microwave canopy scattering model (MIMICS)," *Int. J. Remote Sensing*, vol. 11, no. 7, pp. 1223–1253, 1990.

[6] J. R. Huynen, "Phenomological theory of radar targets," Ph.D. dissertation, Tech. Univ., Delft, The Netherlands, 1970.

[7] J. J. van Zyl, "Unsupervised classification of scattering behavior using radar polarimetry data," *IEEE Trans. Geosci. Remote Sensing*, vol. 27, pp. 36–45, Jan. 1989.

[8] S. R. Cloude, "Uniqueness of target decomposition theorems in radar polarimetry," in *Direct and Inverse Methods in Radar Polarimetry*, Part 1, NATO-ARW, Boerner *et al.*, Eds. Norwell, MA: Kluwer, 1992, pp. 267–296, ISBN 0-7293-1498-0.

[9] W. A. Holm and R. M. Barnes, "On radar polarization mixed state decomposition theorems," in *Proc. 1988 USA Nat. Radar Conf.*, pp. 248–254.

[10] J. J. van Zyl, "Application of Cloude's target decomposition theorem to polarimetric imaging radar data," *Radar Polarimetry*, San Diego, CA, SPIE, vol. 1748, pp. 184–212, July 1992.

[11] S. R. Cloude and E. Pottier, "A review of target decomposition theorems in radar polarimetry," *IEEE Trans. Geosci. Remote Sensing*, vol. 34, pp. 498–518, Mar. 1996.

[12] E. Krogager, "Aspects of polarimetric radar imaging," in Ph.D. dissertation, Tech. Univ. Denmark, published Danish Defence Res. Establishment, May 1993.

[13] E. Krogager and A. H. Czyz, "Properties of the sphere, diplane, helix decomposition," in *Proc. 3rd Int. Workshop Radar Polarimetry, JIPR Nantes*, France, Mar. 1995, pp. 106–114.

[14] A. Freeman and S. Durden, "A three-component scattering model to describe polarimetric SAR data," in *Proc. SPIE Conf. Radar Polarimetry*, San Diego, CA, July 1992, pp. 213–224.

[15] M. C. Dobson, F. T. Ulaby, T. LeToan, A. Beaudoin, E. Kasischke, and N. Christensen, "Dependence of radar backscatter on coniferous biomass," *IEEE Trans. Geosci. Remote Sensing*, vol. 30, pp. 412–415, Mar. 1992.

[16] T. LeToan, A. Beaudoin, J. Riom, and D. Guyon, "Relating forest biomass to SAR data," *IEEE Trans. Geosci. Remote Sensing*, Vol. 30, pp. 403–411, Mar. 1992.

[17] J. G. Fleischman, S. Ayasli, E. M. Adams, and D. R. Gosselin, "Foliage penetration experiment: Part I—Foliage attenuation and backscatter analysis of SAR imagery," *IEEE Trans. Aerosp. Electron. Syst.*, vol. 32, pp. 135–144, Jan. 1996.

[18] F. T. Ulaby, D. Held, M. C. Dobson, K. C. McDonald, and T. B. A. Senior, "Relating polarization phase difference of SAR signals to scene properties," *IEEE Trans. Geosci. Remote Sensing*, vol. GE-25, pp. 83–92, Jan. 1987.

[19] K. C. McDonald, personal communication, 1996.

[20] A. Guissard, "Phase calibration of polarimetric radars from slightly rough surfaces," *IEEE Trans. Geosci. Remote Sensing*, vol. 32, pp. 712–714, May 1994.

Anthony Freeman (M'83–SM'94) received the B.Sc. (Hons.) degree in mathematics in 1979 and the Ph.D. degree in astrophysics in 1982, both from the University of Manchester Institute of Science and Technology, Manchester, U.K..

He was with the Marconi Research Centre, Chelmsford, U.K., from 1982 to 1987, working on moving target imaging with SAR, aircraft SAR motion compensation, SAR design studies, and image quality assessment. He then joined the Radar Science and Engineering Section, Jet Propulsion Laboratory, California Institute of Technology, Pasadena, as a Radar Systems Specialist in 1987 and was promoted to Group Supervisor in 1993. He is now the Radar System Manager for the LightSAR project within the Radar Science and Engineering Section. His current research interests are in information extraction from multidimensional SAR image data. He is Principal Investigator on a NASA-sponsored project to map inundation over the entire Amazon Basin using multiseasonal data from the Japanese JERS-1 SAR instrument. He was Manager of the Spaceborne Imaging Radar-C (SIR-C) Outreach program from 1994 to 1996, responsible for developing and promoting materials based on imaging radar for schools and colleges and for developing and promoting applications of radar image data in the commercial remote-sensing area.

Dr. Freeman was awarded the NASA Exceptional Service Medal in 1995 for his role in the success of the SIR-C missions.

Stephen L. Durden received the B.S. degree in electrical engineering and applied mathematics from Rice University, Houston, TX, and the M.S. and Ph.D. degrees in electrical engineering from Stanford University, Stanford, CA.

He is currently with the Technical Staff in the Radar Science and Engineering Section, Jet Propulsion Laboratory (JPL), California Institute of Technology, Pasadena. Since coming to JPL in 1986, he has worked on the NSCAT scatterometer project, the airborne polarimetric SAR program (AIRSAR), the Airborne Rain Mapping Radar (ARMAR), the Airborne Cloud Radar, LightSAR, and various research tasks involving modeling and analysis of radar data. His current work includes radar systems development, classification of wetlands using SAR data, and radar measurement of the atmosphere.